Edge pedestal structure

W. M. Stacey
Fusion Research Center, Georgia Institute of Technology, Atlanta, Georgia 30332

(Received 29 April 2004; accepted 27 August 2004; published online 3 November 2004)

The hypothesis is advanced and it is investigated that, in between or in the absence of edge-localized modes, the structure of the edge pedestal is determined by the transport requirements of plasma particle, momentum and energy balance, and by recycling neutral atoms. A set of "pedestal equations" following from this hypothesis are presented and applied to calculate the edge density, temperature, rotation velocity, and radial electric field profiles in a DIII-D *H* (high)-mode plasma. It is found that a pedestal structure in the density profile and sharp negative peaks in the radial electric field and poloidal velocity just inside the separatrix are predicted as natural consequences of the conservation of particle and momentum, in qualitative and quantitative agreement with measured values. Detailed examination of the calculation reveals a sequence of mechanisms by which the ionization of recycling neutrals affect the structure of the density profile in the edge pedestal. © *2004 American Institute of Physics*. [DOI: 10.1063/1.1808751]

I. INTRODUCTION

A thin region in the edge of tokamak plasmas within which the density and temperatures increase sharply from the values at the separatrix to much larger "pedestal" values have been observed to be intrinsically associated with *H*-(high) mode confinement. Since the radial temperature profiles in tokamaks are found to be relatively "stiff," the achievable central temperatures (and the good performance associated therewith) are thought to be directly related to the achievable pedestal temperatures (e.g., Refs. 1,2).

Thus, the physics that determines the "structure" (width of the steep gradient region and magnitude of the gradients) has been and remains a subject of intensive research. Correlations of the edge structure with various edge and global parameters have been identified experimentally, and a number of possible physical causes have been suggested (e.g., as reviewed in Ref. 3). This work has led to a number of semiempirical, theory-based scaling laws (e.g., Refs. 3–7), but a comprehensive explanation of the physics of the pedestal structure remains elusive.

Recent advances in magnetohydrodynamic (MHD) stability analysis (e.g., Refs. 8–12) have been successful in predicting the limiting magnitude of the pedestal pressure or pressure gradient at which edge-localized modes (ELMs) become unstable, the nested flux surface magnetic field structure is destroyed, and the pedestal collapses. However, the MHD limits are inherently inequality constraints, and there is no reason nor evidence that they should affect the pedestal structure when the pedestal pressure or pressure gradient is less than the limiting value for MHD stability.

Our purpose in this paper is to advance and investigate the hypothesis that between or in the absence of ELMs the pedestal structure in tokamaks is determined entirely by the requirements of plasma particle, momentum, and energy conservation coupled with the recycling of neutral atoms in the edge plasma. This hypothesis that the pedestal structure is determined by plasma transport (i.e., the plasma particle, momentum, and energy balance equations) has evolved in the course of previous work,[13–15] and the hypothesis that recycling neutral atoms play an important role in determining edge structure is motivated by observation of the correlation of the experimental width of the density pedestal and the neutral atom penetration mean-free path.[16–18]

We previously inferred[14] the experimental values of χ and the momentum transfer frequency averaged over the edge pedestal and compared these values with the values predicted using various theories, in the process introducing some flux-gradient-pinch relations embodying the constraints of particle and momentum balance. In this paper we extend these relations and use them to calculate detailed density, temperature, poloidal velocity, and radial electric fields profiles in the edge pedestal.

The outline of the paper is as follows. We first develop the equations that would determine the edge pedestal structure caused by plasma particle, momentum and energy, and neutral atom transport equations in Sec. II. Then these equations are solved for one *H*-mode discharge and the predicted edge structure is compared with the measured edge structure in Sec. III. Results and conclusions are summarized in Sec. IV.

II. THE EDGE PEDESTAL EQUATIONS

A. Local ion pressure gradient scale length

The multifluid particle and momentum equations can be used to obtain a coupled set of equations relating the radial particle fluxes, pressure gradients, and pinch velocities for the different ion species present in the edge of a tokamak plasma in the presence of a recycling source of neutral atoms and neutral beam injection. The particle continuity equation for ion species "*j*" is

$$\nabla \cdot n_j \boldsymbol{v}_j = S_j, \tag{1}$$

where $S_j(r,\theta) = n_e(r,\theta) n_{j0}(r,\theta) \langle \sigma v \rangle_{ion} \equiv n_e(r,\theta) \nu_{ion}(r,\theta)$ is the ionization source rate of ion species j and n_{j0} is the local concentration of neutrals of species j. Taking the flux surface

average of this equation yields $\langle(\nabla\cdot n_j\boldsymbol{v}_j)_r\rangle=\langle S_j\rangle$ because $\langle\nabla\cdot n_j\boldsymbol{v}_j)_\theta\rangle=0$ identically and $\langle\nabla\cdot n_j\boldsymbol{v}_j)_\phi\rangle=0$ by axisymmetry, which allows Eq. (1) to be written as $(\nabla\cdot n_j\boldsymbol{v}_j)_\theta=S_j-\langle S_j\rangle \equiv\tilde{S}_j$. Subtracting $m_j\boldsymbol{v}_j$ times this form of Eq. (1) from the momentum balance equation for ion species j and noting that $(\nabla\cdot n_j\boldsymbol{v}_j)_r\ll(\nabla\cdot n_j\boldsymbol{v}_j)_\theta$ leads to

$$n_j m_j(\boldsymbol{v}_j\cdot\nabla)\boldsymbol{v}_j+\nabla p_j+\nabla\cdot\boldsymbol{\pi}_j = n_j e_j(\boldsymbol{v}_j\times\mathbf{B})+n_j e_j\mathbf{E}+\mathbf{F}_j+\mathbf{M}_j-n_j m_j\nu_{at}^j\boldsymbol{v}_j-m_j\tilde{S}_j\boldsymbol{v}_j, \tag{2}$$

where $\mathbf{F}_j$ represents the interspecies collisional friction, $\mathbf{M}_j$ represents the external momentum input rate, and the last two terms represent the momentum loss rate due to elastic scattering and charge exchange with neutrals of all ion species ''k''$[\nu_{atj}=\Sigma_k n_{k0}^c(\langle\sigma v\rangle_{el}+\langle\sigma v\rangle_{cx})_{jk}]$ and due to the introduction of ions with no net momentum via ionization of a neutral of species j. Only the "cold" neutrals that have not already suffered an elastic scattering or charge-exchange collision in the pedestal are included in ν_{atj}. The development of a general flux-gradient-pinch relationship from these two equations is summarized in Appendix A and treated more fully in Refs. 14,15.

When it is assumed that (i) the plasma contains a main ion species "i" and a single effective impurity species "z" the concentration of which is a constant fraction $f_z=n_z/n_i$ of the main ion concentration, and that (ii) both ion species have the same temperature T_i, Eqs. (1) and (2) reduce (see Appendix A and Ref. 15) to a flux-gradient-pinch relationship for the main ions,

$$-\frac{1}{p_i}\frac{dp_i}{dr}\equiv L_{pi}^{-1}=\frac{\Gamma_i/n_i-v_{pi}}{\hat{D}_i}\equiv\frac{v_{ri}-v_{pi}}{\hat{D}_i}, \tag{3}$$

where Γ_i is the radial particle flux. The effective diffusion coefficient is [with reference to Eqs. (A2)]

$$\hat{D}_i\equiv D_{ii}-D_{iz}=\frac{m_i T_i\nu_{iz}}{(e_i B_\theta)^2}\left[1+\frac{\nu_{di}^*}{\nu_{iz}}-\frac{1}{\langle Z\rangle}\right], \tag{4}$$

where ν_{iz} is the interspecies collision frequency, ν_{di}^* is the viscous plus atomic physics (charge-exchange, elastic scattering, ionization) frequency for the radial transfer of toroidal momentum [see Eqs. (A4)–(A6)], and $\langle Z\rangle$ is the average local charge state of the impurity species. The remaining collection of quantities entering this relationship is identified as the "pinch" velocity

$$v_{pi}=\frac{1}{e_i B_\theta}[-M_{\phi i}/n_i-e_i E_\phi^A+m_i\nu_{di}^*(E_r/B_\theta+f_p^{-1}v_{\theta i}) + m_i\nu_{iz}f_p^{-1}(v_{\theta i}-v_{\theta z})], \tag{5}$$

where M_φ and E_φ^A are the toroidal components of the input momentum rate and the induced electric field, E_r is the radial electric field, v_θ is the poloidal rotation velocity, and $f_p=B_\theta/B_\varphi$.

An expression for calculating the radial electric field can be derived by summing the toroidal component of the momentum balance equation for all species and using the radial component of the momentum balance equation $v_{\varphi j}=f_p^{-1}v_{\theta j}+E_r/B_0-(dp_j/dr)/(n_j e_j B_0)$ to obtain (see Appendix A and Ref. 19)

$$\frac{E_r}{B_\theta}=\frac{\sum_{ions}[M_{\phi j}-n_j m_j\nu_{dj}^*\{f_p^{-1}v_{\theta j}-(dp_j/dr)/(n_j e_j B_\theta)\}]}{\sum_{ions}n_j m_j\nu_{dj}^*}. \tag{6}$$

The poloidal rotation velocities for the main ions and impurities, along with the sine (n_j^s) and cosine (n_j^c) components of the ion and impurity density poloidal variation over the flux surface (needed to calculate the gyroviscous component ν_{di} of ν_{di}^*—see Appendix A), are calculated by taking the low order Fourier moments of the poloidal components of the momentum balance equations for the main ions and impurities,[15,20]

$$\langle X\mathbf{n}_\theta\cdot\mathbf{Eq2_j}\rangle=0,\quad X=1,\sin\theta,\cos\theta,\quad j=i,z, \tag{7}$$

where $\mathbf{Eq2_j}$ denotes the momentum balance Eq. (2) for species $j=i,z$ and $\langle\ \rangle$ denotes a flux surface average. Equations (7) are given explicitly by Eqs. (A10)–(A12) in Appendix A.

B. Local temperature and density gradient scale lengths

The local heat conduction relation $q_j=-n_j\chi_j dT_j/dr, j=i,e$, can be used to express the local ion and electron temperature gradient scale lengths, $L_{Tj}^{-1}\equiv-T_j/(dT_j/dr)$, in terms of the respective local total heat fluxes, Q_j, and convective heat fluxes, $5/2T_j\Gamma_j$:

$$L_{Tj}^{-1}=\frac{1}{\chi_j}\left[\frac{Q_j}{n_j T_j}-\frac{5}{2}\frac{\Gamma_j}{n_j}\right],\quad j=i,e. \tag{8}$$

The inverse ion density gradient scale length may then be determined by subtracting the inverse ion temperature gradient scale length of Eq. (8) from the inverse ion pressure gradient scale length given by Eq. (3):

$$L_{ni}^{-1}=L_{pi}^{-1}-L_{Ti}^{-1}. \tag{9}$$

C. Local particle and heat fluxes

With reference to the discussion following Eq. (1), the local flux surface averaged particle balance equation for the main ion particle flux in the edge region can be written

$$\frac{d\Gamma_i}{dr}=n_e\nu_{ioni}+n_i\nu_{ionb},\quad \Gamma_i(r_{sep})=\Gamma_i^{sep}, \tag{10}$$

where ν_{ioni} and ν_{ionb} are the frequencies for the ionization by electron impact of recycling neutral atoms of the main ion species and for ionization of neutral beam injected particles, respectively. In order to solve this equation it is necessary to specify a boundary condition either at the separatrix or at some radius interior to the pedestal location. Because we are interested in calculating profiles from the separatrix inward and because we can determine the particle flux crossing the separatrix from a particle balance on the region inside the separatrix, we choose to specify the (net outward) ion particle flux crossing the separatrix, Γ_{sepi}, as the boundary con-

dition and to numerically integrate this equation inward from the separatrix to determine the local particle flux within the edge region of interest.

The ion and electron heat fluxes in the edge region satisfy the energy balance equations,

$$\frac{dQ_i}{dr} = -\frac{3}{2}T_i n_e \nu_{ati} - \dot{Q}_{ie} + \dot{Q}_{nbi}, \quad Q_i(r_{sep}) = Q_i^{sep} \tag{11}$$

and

$$\frac{dQ_e}{dr} = -E_{ion} n_e \nu_{ioni} - n_e n_z L_z + \dot{Q}_{ie} + \dot{Q}_{n_{be}},$$
$$Q_e(r_{sep}) = Q_e^{sep}, \tag{12}$$

where $\dot{Q}_{ie}$ is the rate of collisional energy transfer from ions to electrons, $\dot{Q}_{nbi,e}$ is the rate of energy deposition in the ions or electrons by injected neutral beams (or any other form of heating), ν_{ati} is the frequency of charge exchange plus elastic scattering of cool recycling neutral atoms which have not previously suffered a collision in the scrape-off layer (SOL) or edge region, E_{ion} is the ionization energy, and L_z is the radiation emissivity of the impurity ions (which is calculated with a coronal equilibrium model using the local electron density and temperature, taking into account the enhancement due to charge exchange and recombination with the recycling neutrals). For reasons similar to those discussed above for the ion particle flux, we specify the values of the ion and electron heat fluxes at the separatrix as boundary conditions and numerically integrate Eqs. (11) and (12) inward from the separatrix into the edge region. The total heat flux at the separatrix, $Q^{sep} = Q_i^{sep} + Q_e^{sep}$, can be determined from a power balance on the region inside the separatrix, but the split between ion and electron heat flux is generally unknown experimentally.

Penetration of the inward flux of recycling neutrals, $J^+(r)$, into the edge region is calculated using an interface-current-balance method,[21] using as a boundary condition the recycling neutral current $J^+(r_{sol}) = J_{sol}^+$, passing inward across the outer boundary of the scrape-off layer. The inward (+) and outward (−) partial currents at successive interfaces r_n and r_{n+1} are related by

$$J_+(r_{n+1}) = T_n J_+(r_n) + R_n J_-(r_{n+1}),$$
$$J_-(r_n) = T_n J_-(r_{n+1}) + R_n J_+(r_n), \quad n = 1, 2 \cdots N, \tag{13}$$

where T_n is the probability that a neutral atom is transmitted through the interval $\Delta_n = r_{n+1} - r_n$ without a collision and $2R_n$ is the probability that a neutral atom (or its neutral progeny via charge-exchange) that does have one or more collisions in the interval Δ_n ultimately escapes from the interval across the interface at r_n or r_{n+1}. These quantities are defined in Appendix B, where the computational algorithm is given, and the theoretical development is described in detail in Ref. 21.

Two groups of neutrals are treated: (i) cold neutrals which have recycled from the wall and penetrate across the SOL and into the separatrix with a temperature characteristic of the wall recycling atoms; and (ii) neutrals that have undergone one or more charge exchange or scattering collisions in the SOL or pedestal regions and take on the local ion temperature as a result. The first group of neutrals is used to compute the cold neutral density that is used to evaluate ν_{ati}, while both groups contribute to ν_{ioni}.

D. Density and temperature profiles in the plasma edge

The ion density profile and the ion and electron temperature profiles in the plasma edge are calculated by numerically integrating the defining relations for the respective inverse gradient scale lengths inward from the separatrix,

$$-\frac{1}{n_i}\frac{dn_i}{dr} = L_{ni}^{-1} = L_{pi}^{-1} - L_{Ti}^{-1} = \frac{\mathrm{v}_{ri} - \mathrm{v}_{pi}}{\hat{D}_i} - L_{Ti}^{-1},$$
$$n_i(r_{sep}) = n_i^{sep}, \tag{14}$$

$$-\frac{1}{T_i}\frac{dT_i}{dr} = L_{Ti}^{-1} = \frac{1}{\chi_i}\left[\frac{Q_i}{n_i T_i} - \frac{5}{2}\frac{\Gamma_i}{n_i}\right], \quad T_i(r_{sep}) = T_i^{sep}, \tag{15}$$

and

$$-\frac{1}{T_e}\frac{dT_e}{dr} = L_{Te}^{-1} = \frac{1}{\chi_e}\left[\frac{Q_e}{n_e T_e} - \frac{5}{2}\frac{\Gamma_e}{n_e}\right], \quad T_e(r_{sep}) = T_e^{sep} \tag{16}$$

subject to a separatrix boundary condition.

The neutral atom density profile in the plasma edge is calculated from the attenuating current of neutral atoms by equating the local divergence in total neutral flux to the ionization rate, $dJ/dr = n_{oi} n_e \langle \sigma v \rangle$, and the cold neutral atom density profile is calculated from the local attenuated cold neutral atom flux $J_+^{\mathrm{cold}} = n_o v_o^{\mathrm{cold}}$.

E. Boundary conditions for edge plasma profile calculations

In order to solve Eqs. (10)–(16) for the profiles in the edge plasma it is necessary to specify the indicated separatrix boundary conditions on density, temperature, particle, heat fluxes, and the SOL inward recycling neutral flux boundary condition. For this purpose we have embedded the above edge plasma calculation within a global code[22] which: (i) performs core plasma particle and power balance calculations (including radiative cooling and recycling neutral influx) to determine outward plasma particle and heat fluxes across the separatrix into the SOL which (ii) are input to a "two-point" divertor model (including radiative and atomic physics cooling, particle sources, and momentum sinks) to calculate plasma density and temperature on the separatrix at the midplane and at the divertor plate and to calculate the plasma flux to the divertor plate which (iii) creates the recycling source of neutral molecules and atoms for a two-dimensional (2D) neutral transport recycling calculation[23] throughout the divertor and plasma chamber that provides the neutral influx for the core particle balance calculation. Thus, the global code can calculate all of the boundary con-

ditions needed for the edge plasma calculation, although the present code does not distinguish between T_e^{sep} and T_i^{sep} nor does it provide separate Q_e^{sep} and Q_i^{sep}.

When the global code is used for experimental analysis, experimental values of n_e^{sep}, T_e^{sep}, and T_i^{sep} are normally used as input, and the gas fueling source is adjusted until the calculated line average density matches the measured values, in order to "normalize" the neutral recycling fueling calculation to experiment.

For the edge plasma calculations reported in the following section, experimental values of n_e^{sep}, T_e^{sep}, and T_i^{sep}, particle and power balance calculated values of Γ_i^{sep} and $Q^{sep} = Q_i^{sep} + Q_e^{sep}$, and J_{sol}^{+} from the 2D neutral recycling calculation are used.

III. CALCULATION OF EDGE PROFILES IN A DIII-D SHOT

The equations described in the preceding section were solved numerically for DIII-D shot #92976 at a time (3210 ms) well into the *H*-mode phase of the discharge. This was a heavily gas-fueled ($\approx$80 Torr l/s) shot characterized by the parameters ($I=1.0$ MA, $B=-2.1$ T, $P_{nb}=5.0$ MW, $R=1.71$ m, $a=0.6$ m, $\kappa=1.78$, $q_{95}=5.7$) with a carbon impurity concentration in the edge of $f_z=0.025$. The experimental values of n_e^{sep}, T_e^{sep}, and T_i^{sep}, the particle and power balance values of Γ_i^{sep} and $Q_i^{sep}+Q_e^{sep}$ (with the further assumption $Q_i^{sep}=Q_e^{sep}$), and the value of the recycling neutral influx J_{sol}^{+} calculated by the global code were used as boundary conditions for the pedestal calculations. The experimental values of $v_{\varphi \text{carbon}}$ were used for $v_{\varphi i}$ and $v_{\varphi z}$ (and to evaluate $L_{v\varphi}^{-1}$). Based on previous experience,[14] the thermal conductivities were modeled as $\chi_i = 2\chi_{ch}^{os} + \chi_{itg}$ and $\chi_e = \chi_{etg} + \chi_{edw}$ in order to match values inferred from experiment, where χ_{ch}^{os} is the Chang–Hinton expression corrected for orbit squeezing ($\chi_{ch}^{os} = \chi_{ch}/S^{3/2}$ where S is a factor that accounts for orbit squeezing in the presence of a strong shear in E_r), χ_{itg} is an ion temperature gradient (ITG) mode expression, χ_{etg} is an electron temperature gradient (ETG) mode expression, and χ_{edw} is an electron drift wave (EDW) (or TEM) expression (see Appendix C). For consistency, we also correct the diffusion coefficient of Eq. (4) for orbit squeezing, $\hat{D}_i^{os} = \hat{D}_i/S^{3/2}$. Neoclassical gyroviscosity was used to evaluate ν_{di} and a neoclassical model for the parallel viscosity was used (Appendix A).

A. Density and temperature profiles

The calculated density and temperature profiles in the edge pedestal region are compared with measured data in Figs. 1–3. There is a sharp pedestal structure in both the calculated and measured electron densities and distinct but somewhat less dramatic pedestal structures in the electron and ion temperature data and calculations.

The agreement is sufficiently good to support the conclusion that the solution of the "pedestal equations" of the preceding section can describe the pedestal structure at this time in this discharge. (We could improve the agreement by adjusting the transport coefficients, but refrained from doing this.) This result provides one point of support for our hypothesis that between or in the absence of ELMs the structure of the *H*-mode pedestal in tokamaks is determined entirely by the requirements of plasma particle, momentum, and energy conservation coupled with the recycling of neutral atoms in the edge plasma.

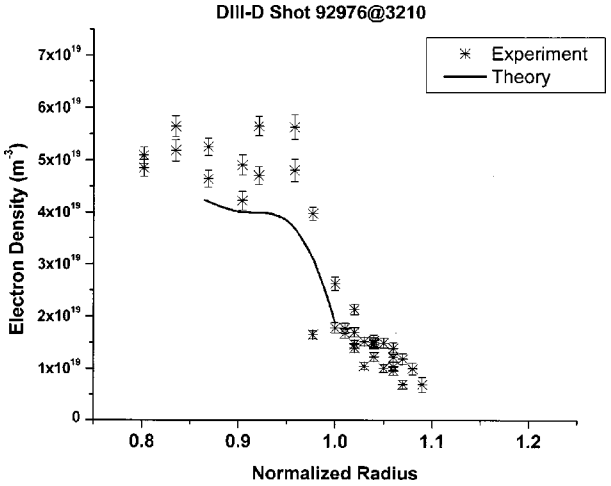

FIG. 1. Measure and calculated electron densities in the edge of a DIII-D *H*-mode shot.

Now we examine the details, but first a cautionary note. Since the pedestal equations of the preceding section are highly coupled nonlinear equations, it is difficult to identify what is the "cause" and what is the "effect," although some interesting relationships can certainly be identified.

B. Factors determining the ion pressure gradient

The normalized ion pressure gradient, L_{pi}^{-1}, and the terms determining it in Eq. (3) are plotted in Fig. 4, except for $\hat{D}_i$ which decreased from ≈ 1 m^2/s at $\rho=0.865$ to ≈ 0.4 m^2/s just inside the separatrix ($\rho=1.0$). L_{pi}^{-1} peaks sharply just inside the separatrix, which is caused in part by the fact that the ion radial velocity, $v_{ri}=\Gamma_i/n_i$, peaks just inside the separatrix due (i) to an increase with radius (by a factor of about

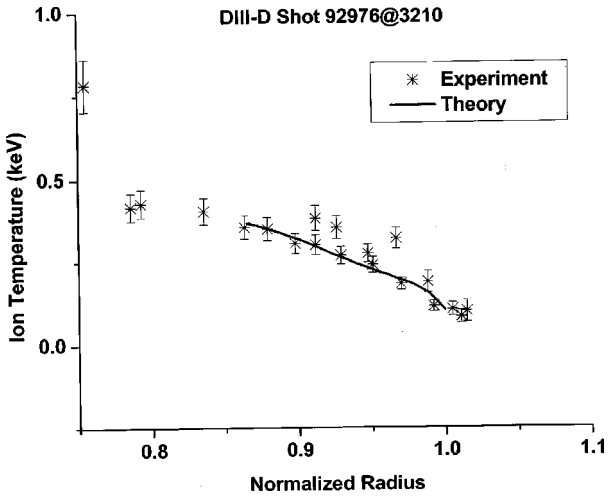

FIG. 2. Measure and calculated ion temperatures in the edge of a DIII-D *H*-mode shot.

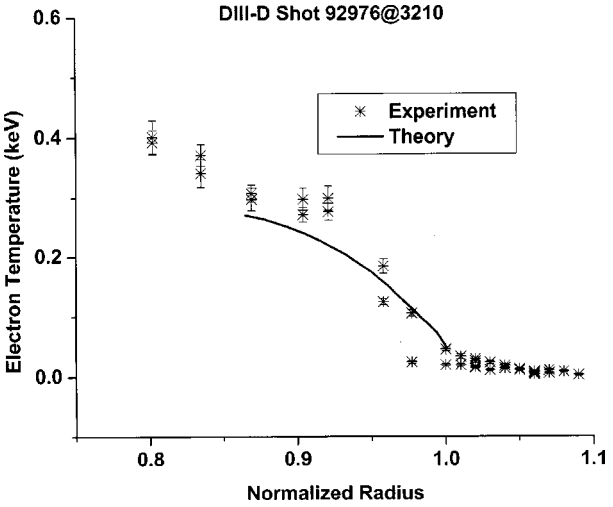

FIG. 3. Measure and calculated electron temperatures in the edge of a DIII-D *H*-mode shot.

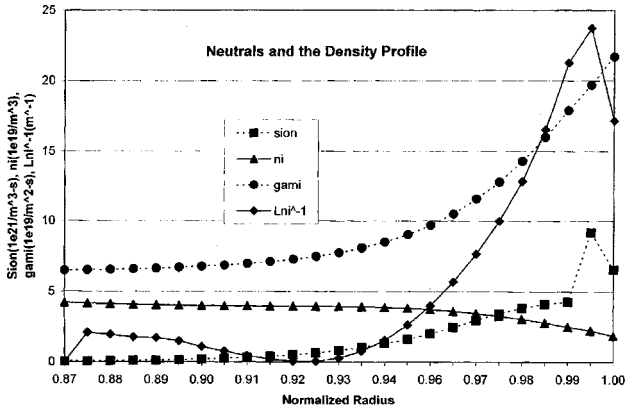

FIG. 5. Relation of recycling neutral atom ionization source and the edge density profile in the edge of a DIII-D *H*-mode shot.

3.5 over the calculation interval inside the separatrix) of Γ_i due to ionization of recycling neutrals and (ii) to the sharp decrease in n_i just inside the separatrix.

The increase in v_{ri}, and hence L_{pi}^{-1}, as the separatrix is approached from inside contributes to a sharp increase in magnitude of the negative poloidal velocity [see Eq. (A10)], as may be seen in Fig. 4. The strong increases in negative poloidal rotation and in negative pressure gradients produce a strong negative peak in the radial electric field of Eq. (6) just inside the separatrix ($f_p<0$). (The calculated E_r becomes positive for $\rho<0.95$ and has not been plotted to avoid difficulty with the logarithmic scale.)

The inward pinch velocity given by Eq. (5) and plotted in Fig. 4 was primarily determined by the toroidal electric field E_φ and friction ν_{iz} terms well inside the separatrix. However, the momentum drag ν_{di}^* term involving the strongly peaked radial electric field and the poloidal rotation velocity became dominant and caused the sharp inward (negative) spike just inside the separatrix. This large inward (negative) pinch velocity just inside the separatrix further contributes to the large negative pressure gradient of Eq. (3) just inside the separatrix and would seem to be the cause of the particle "transport barrier" in the edge pedestal.

The sharp negative spikes in v_{0z} (the carbon poloidal velocity profile was calculated to be similar to, but of slightly larger negative magnitude than, the deuterium poloidal velocity profile shown in Fig. 4) and E_r are characteristic features observed in *H*-mode pedestals. The measured values just inside the separatrix in this shot were $v_{\theta z} \approx -(5\text{–}10)$km/s and $E_r \approx -13$ kV/m, which are similar to the calculated results in Fig. 4.

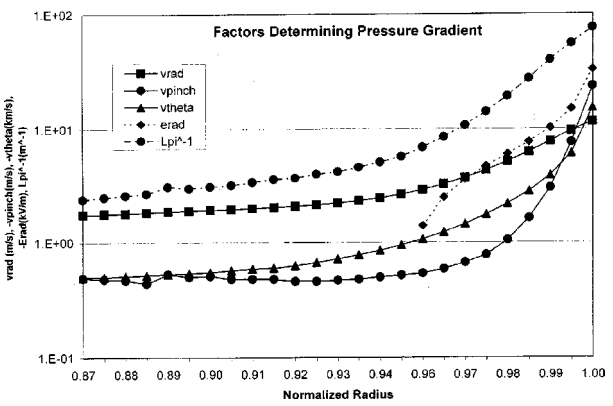

FIG. 4. Factors determining the ion pressure gradient in the edge of a DIII-D *H*-mode shot.

C. Factors determining the ion density gradient

The ion temperature gradient also affects the determination of the ion density profile. The calculated ion density profile (and the electron density profile also in this $f_z = n_z/n_i = \text{const}$ model) is directly determined via integration of Eq. (14) by $L_{ni}^{-1} = L_{pi}^{-1} - L_{Ti}^{-1}$. For this shot, the calculated $L_{pi}^{-1} \approx L_{Ti}^{-1}$ for $0.87<\rho<0.94$, but the calculated L_{pi}^{-1} was significantly larger than the calculated L_{Ti}^{-1} for $0.94<\rho<1.0$, resulting in a steep ion density gradient over $0.94<\rho<1.0$ but a relatively small density gradient over $0.87<\rho<0.94$. The calculated ion density profile and the calculated ion density gradient producing it are shown in Fig. 5. The factors determining the calculated L_{pi}^{-1} were discussed in the preceding Sec. III B. The factors determining L_{Ti}^{-1} are given in Eq. (8). $\chi_i = 2\chi_{ch}^{os} + \chi_{itg}$ decreased by ≈ 3, Q_i decreased by a factor of 2, and Γ_i decreased by ≈ 3 between $\rho = 0.87$ and $\rho = 1.0$, and n_i and T_i varied as shown in Figs. 2 and 5.

It has been hypothesized[16–18] that neutral penetration may cause the width of the density pedestal, which extends over $\approx 0.94<\rho<1.0$ for this shot. To further examine this hypothesis, we plot the calculated ionization source S_i and the ion particle flux Γ_i in Fig. 5. S_i does increase with increasing ρ just inside the separatrix, and the combination of n_i decreasing with ρ and n_{oi} increasing with ρ produces a peak just inside the separatrix. This causes the ion flux Γ_i to increase more rapidly with ρ just inside the separatrix where S_i is largest. The sequence of mechanisms by which this increase in Γ_i due to ionization affect the ion pressure gradient was discussed in the preceding section. Ionization and

charge exchange could also affect the temperature profiles, thereby having an effect on the density profile.

We note that all calculations were carried out using a flux surface averaged model employing a neutral influx that was a weighted average of the influxes from the *X*-point region and from the mid-plane region. Since the flux surfaces are more widely separated in the *X*-point region, the dominant *X*-point influx would actually attenuate more rapidly in ρ than was calculated in this flux surface average model, resulting in the rapid variation in S_i and Γ_i being concentrated somewhat closer to the separatrix than is indicated in Fig. 5.

IV. SUMMARY AND CONCLUSIONS

We have examined the hypothesis that, between and in the absence of ELMs, the edge pedestal structure (gradients in density and temperature and the widths over which they extend) are determined by the transport requirements of plasma particle, momentum and energy balance, and by recycling neutral atoms. A set of pedestal equations was developed based on this hypothesis and applied to calculate density, temperature, and other profiles in the edge region of a DIII-D *H*-mode tokamak plasma. The calculated density and temperature profiles exhibited an edge pedestal structure and were in reasonable quantitative agreement with the experimental profiles. The calculated profiles of radial electric field and poloidal rotation velocity exhibited sharp negative peaking just inside the separatrix, also in reasonable quantitative agreement with experiment. All of these calculated pedestal profile features were the natural consequence of particle, momentum and energy balance, and of neutral particle recycling. The only "external" input to these calculations were the thermal transport coefficients, which were chosen to yield values close to those inferred from experiment.

Detailed examination of the calculation indicated that the plasma ion pressure gradient was produced by the difference of the total ion radial velocity and the inward (negative) radial ion pinch velocity, both of which were peaked just inside the separatrix. The peaking in the total radial velocity was due to the buildup of radial ion flux with increasing radius due to ionization of recycling neutral atoms and to the decrease in ion density. This peaking in the radial ion velocity just inside the separatrix apparently was the cause of the negative peaking of the ion and impurity poloidal velocities in the same location, which in turn were the cause of the negative peaking in the radial electric field. The negative peaking in ion poloidal velocity and radial electric field appear to be the cause of the peaking in the inward (negative) pinch velocity, which in turn was the principal cause of the sharp ion pressure gradient just inside the separatrix. This sequence of events appears to be the mechanism by which the ionization of recycling neutrals affects the density profile in the edge pedestal.

The ion and electron temperature gradients, calculated from the respective heat conduction requirements, were also large and negative just inside the separatrix and diminished in magnitude for smaller ρ, leading to a modest pedestal structure in the respective temperature profiles. The (negative) ion temperature gradient was comparable to the ion pressure gradient inside of $\rho \approx 0.94$, but was smaller in magnitude for $\rho > \approx 0.94$. When the ion temperature gradient was subtracted from the ion pressure gradient, the resulting ion density gradient was very small for $\rho < \approx 0.94$ but large for $\rho > \approx 0.94$, producing a strong pedestal structure in the ion (and electron) edge density profile.

Clearly, the edge pedestal equations of this paper need to be applied to the calculation of edge profiles in a wide variety of shots with different edge parameters, heating powers, neutral recycling levels, etc., both to confirm the validity of the hypothesis on which they are based and to better understand the very complex interactions that determine the observed edge pedestal structure in tokamaks. We intend to make such calculations in the future.

The question of whether the same set of equations can describe "internal transport barriers" observed in tokamaks naturally arises. The same equations should describe internal transport barriers, but obviously the recycling neutral atoms and impurity radiation will be less important and the particle, momentum, and energy sources due to neutral beams and any rf heating source will be more important. The effects of ion radial and poloidal rotation and the radial electric field, which were found to be so important in the edge, are not at all clear for an internal transport barrier. Furthermore, the heat conductivities might be quite different in the core than in the edge.

The three most significant findings of this paper are as follows.

(1) The demonstration that the density pedestal structure of the edge pedestal seems to be a natural consequence of the requirements of particle, momentum, and energy balance, together with neutral recycling.
(2) The identification of the involved sequence of mechanisms by which the ionization of recycling neutrals affects the edge pedestal structure.
(3) The identification of a prescription for the pinch velocity and a demonstration of its importance in determining edge particle transport and the edge density pedestal structure.

These results have important implications for how the edge pedestal should be modeled. We note that 2D edge codes, which treat particle transport with diffusive models and neglect momentum transport inside the separatrix, routinely calculate an edge density pedestal by adjusting the diffusion coefficient to do so, but our results indicate that the pinch velocity (which is usually neglected or treated on an *ad hoc* basis in such codes) is dominant in determining the density pedestal. This calls into question the physical meaningfulness of these pedestal predictions. The present model avoids the necessity for using *ad hoc* discontinuities or near discontinuities in transport coefficients to model the pedestal region.

The present results also call into question the physical meaningfulness of the more ambitious recent effort to model the pedestal by combining a diffusive plasma density model and an *ad hoc* neutral model,[16,18] again because of the omis-

sion of the pinch velocity and other requirements of momentum conservation, which appear to dominate in the determination of the pedestal structure.

APPENDIX A: FLUX-GRADIENT RELATIONS FROM PARTICLE AND MOMENTUM BALANCE

1. Pressure gradient

It has been shown previously[15] that the momentum and particle balance equations for a multispecies tokamak plasma can quite generally be solved to obtain a coupled set of equations relating the particle fluxes, the pressure gradients, and the "pinch velocities" for the various species

$$\Gamma_j = n_j D_{jj}(L_{nj}^{-1} + L_{Tj}^{-1}) - n_j D_{jk}(L_{nk}^{-1} + L_{Tk}^{-1}) + n_j v_{pj}, \tag{A1}$$

where the "diffusion coefficients" are given by

$$D_{jj} \equiv \frac{m_j T_j (\nu_{dj}^* + \nu_{jj})}{(e_j B_\theta)^2}, \quad D_{jk} \equiv \frac{m_j T_k \nu_{jk}}{e_j e_k B_\theta{}^2}, \tag{A2}$$

the pinch velocities are given by

$$n_j v_{pj} \equiv -\frac{\overline{M}_{\phi j}}{e_j B_\theta} - \frac{n_j \overline{E}_\phi^A}{B_\theta} + \frac{n_j m_j \nu_{dj}^*}{e_j B_\theta}\left(\frac{E_r}{B_\theta}\right) + \frac{n_j m_j f_p^{-1}}{e_j B_\theta}[(\nu_{jk} + \nu_{dj}^*)\overline{v}_{\theta j} - \nu_{jk}\overline{v}_{\theta k}], \tag{A3}$$

and where a sum over the $k \neq j$ terms is understood. Here, ν_{jk} is the interspecies j-k collision frequency, M_φ and $E_\varphi^{\ A}$ denote the toroidal components of the momentum input and the induced electric field, $L_{pj}^{-1} \equiv -(dp_j/dr)/p_j$, v_{rj} and $v_{\theta j}$ denote the radial and poloidal components of the velocity of species j averaged over the flux surface, $f_p \equiv B_\theta/B_\varphi$, the total momentum transfer, or "drag," frequency $\nu_{dj}^{\ *}$ is given by

$$\overline{\nu}_{dj}^* \equiv \overline{\nu}_{dj} + \overline{\nu}_{atj} + \overline{\nu}_{ionj}\xi_j, \tag{A4}$$

which consists of a cross-field viscous momentum transport frequency formally given by

$$\overline{\nu}_{dj} \equiv \langle R^2 \nabla \phi \cdot \nabla \cdot \boldsymbol{\pi}_j \rangle / \overline{R n_j} m_j \overline{v}_{\phi j} \tag{A5}$$

and of "atomic physics" (charge exchange plus elastic scattering) and ionization momentum loss terms, with the neutral ionization source poloidal asymmetry characterized by

$$\xi_j \equiv \langle R^2 \nabla \phi \cdot m_j \tilde{S}_j v_{\phi j} \rangle / \overline{R} m_j \overline{S}_j \overline{v}_{\phi j}, \tag{A6}$$

where $S_j(r,\theta) = n_e(r,\theta) n_{j0}(r,\theta) \langle \sigma v \rangle_{ion} \equiv n_e(r,\theta)\nu_{ion}(r,\theta)$ is the ionization source rate of ion species j, n_{j0} is the local concentration of neutrals of species j, and $v_{\varphi j}$ is the toroidal component of the velocity of species j.

2. Viscous cross-field momentum transport

In order to actually evaluate the above equations it is necessary to specify the toroidal viscous force $\langle R^2 \nabla \phi \cdot \nabla \cdot \pi \rangle$, which determines the viscous momentum transport frequency ν_{dj}, given by Eq. (A5). There are three neoclassical viscosity components—parallel, perpendicular, and gyroviscous. The "parallel" component of the neoclassical viscosity vanishes identically in the viscous force term, and the "perpendicular" component is several orders of magnitude smaller than the "gyroviscous" component[24]

$$\langle R^2 \nabla \phi \cdot \nabla \cdot \pi_j \rangle = \frac{1}{2}\tilde{\theta}_j G_j \frac{n_j m_j T_j}{e_j B_\phi}\frac{v_{\phi j}}{\overline{R}} \equiv R n_j m_j \nu_{dj} v_{\phi j}, \tag{A7}$$

where

$$\tilde{\theta}_j \equiv (4 + \tilde{n}_j^c)\tilde{v}_{\phi j}^s + \tilde{n}_j^s(1 - \tilde{v}_{\phi j}^c) = (4 + \tilde{n}_j^c)\left[-(\hat{v}_{\theta j}/\hat{v}_{\phi j})(\tilde{\Phi}^s + \tilde{n}_j^s) + \tilde{\Phi}^s\right] + \tilde{n}_j^s\left[(\hat{v}_{\theta j}/\hat{v}_{\phi j})(2 + \tilde{\Phi}^c + \tilde{n}_j^c) - \tilde{\Phi}^c\right] \tag{A8}$$

represents poloidal asymmetries and

$$G_j \equiv -\frac{r}{\eta_{4j} v_{\phi j}}\frac{\partial(\eta_{4j} v_{\phi j})}{\partial r} = r(L_{pj}^{-1} + L_{v\phi j}^{-1}) \tag{A9}$$

with the gyroviscosity coefficient $\eta_{4j} \approx n_j m_j T_j / e_j B$ and $L_x^{\ -1} = -(dx/dr)/x$.

3. Poloidal velocities and density asymmetries

In order to evaluate Eq. (A8) it is first necessary to calculate the sine and cosine components of the density and toroidal velocity poloidal variations over the flux surface. Using a low-order Fourier expansion of the poloidal dependence of the densities and rotation velocities over the flux surface in the poloidal component of the momentum balance equation and taking the flux surface average with 1, $\sin\theta$, and $\cos\theta$ weighting then yields a coupled set of three nonlinear moments equations per species that can be solved numerically for the flux surface average poloidal velocities and the sine and cosine components of the density variations, for the various ion species present, over the flux surface.[15,20]

$$\begin{aligned}
&\hat{v}_{\theta j}\Bigg[-q\hat{v}_{\phi j}\varepsilon(\tilde{n}_j^s + \tilde{\Phi}^s) - q^2 f_j f_p\left(1 + \tilde{\Phi}^c + \frac{2}{3}\tilde{n}_j^c\right) + f_p\sum_{k\neq j}\nu_{jk}^* \\
&\quad + \frac{q}{\varepsilon}\nu_{atj}^* f_p + \frac{1}{2}f_p\varepsilon\nu_{ionj}^*\Bigg\{(1 + \tilde{n}_j^c)\left[\frac{\overline{n}_e}{\overline{n}_j}(\tilde{n}_e^c + \tilde{n}_{oj}^c) - (\tilde{n}_j^c + \tilde{n}_{oj}^c)\right] + \tilde{n}_j^s\left[\frac{\overline{n}_e}{\overline{n}_j}(\tilde{n}_e^s + \tilde{n}_{oj}^s) - (\tilde{n}_j^s + \tilde{n}_{oj}^s)\right]\Bigg\}\Bigg] \\
&\quad - \sum_{k\neq j}\upsilon_{k\theta}\left[f_p\nu_{jk}\sqrt{\frac{m_j}{m_k}}\right] \\
&= -\hat{v}_{rj} - q\varepsilon\frac{1}{4}\tilde{n}_j^s - q\varepsilon\hat{\Phi}_j\left[\frac{1}{4}(\tilde{\Phi}^s + \tilde{n}_j^c\tilde{\Phi}^s - \tilde{n}_j^s\tilde{\Phi}^c)\right] \\
&\quad - q^2 f_j f_p(\hat{v}_{\phi j} + \widehat{P_j'})\tilde{\Phi}^c - q\varepsilon\hat{v}_{\phi j}\left[(\hat{v}_{\phi j} + \widehat{P_j'})\tilde{\Phi}^s + \frac{1}{2}\hat{v}_{\phi j}\tilde{n}_j^s\right] \\
&\quad - \frac{\overline{n}_e}{\overline{n}_j}\nu_{ionj}^* q\left[\hat{v}_{\phi j}\varepsilon(\tilde{n}_e^c + \tilde{n}_{oj}^c) - \frac{2}{3}q f_j(\tilde{n}_e^s + \tilde{n}_{oj}^s)\right],
\end{aligned} \tag{A10}$$

$$\tilde{n}_j^s\left[\frac{1}{3}\frac{q^2}{\varepsilon}f_j f_p\hat{v}_{\theta j}+\frac{1}{2}\varepsilon\hat{v}_{rj}-\frac{1}{2}\varepsilon f_p\sum_{k\neq j}\nu_{jk}^*\hat{v}_{\theta k}\sqrt{\frac{m_j}{m_k}}+\frac{1}{2}q\nu_{ion}^*f_p\hat{v}_{\theta j}\right]$$
$$+\tilde{n}_j^c\left[\frac{1}{2}qf_p^2\hat{v}_{\theta j}^2-\frac{1}{4}q+\frac{1}{2}q\nu_{atj}^*\nu_{ionj}^*\right]$$
$$=-\frac{1}{2}\varepsilon f_p\sum_{k\neq j}\nu_{jk}^*\hat{v}_{\theta j}\tilde{n}_k^s-\frac{1}{4}q\hat{\Phi}_j[-\overline{\Phi}^c]$$
$$-\frac{q^2}{\varepsilon}f_j f_p\left[\frac{1}{2}(\hat{v}_{\theta j}-\hat{v}_{\phi j}-\widehat{P'}_j)\tilde{\Phi}^s-\frac{1}{2}qf_p^2\hat{v}_{\theta j}^2-\frac{1}{2}q\hat{v}_{\phi j}^2\right.$$
$$-\frac{1}{2}q\nu_{atj}^*[f_p\hat{v}_{\theta j}\tilde{n}_{oj}^s+\nu_{ionj}^*\tilde{n}_{oj}^c]$$
$$-q\nu_{ionj}^*f_p\left[\frac{1}{2}\hat{v}_{\theta j}\left\{\tilde{n}_{oj}^s\left(1+\frac{\overline{n_e}}{\overline{n_j}}\right)+\frac{\overline{n_e}}{\overline{n_j}}\tilde{n}_e^s\right\}\right.$$
$$\left.\left.+\frac{1}{3}\frac{q}{\varepsilon}f_j\frac{\overline{n_e}}{\overline{n_j}}(\tilde{n}_e^c+\tilde{n}_{oj}^c)\right]\right], \tag{A11}$$

and

$$\tilde{n}_j^c\left[\frac{1}{3}\frac{q^2}{\varepsilon}f_j f_p\hat{v}_{\theta j}+\frac{1}{2}\varepsilon\hat{v}_{rj}-\frac{1}{2}\varepsilon f_p\sum_{k\neq j}\nu_{jk}^*\hat{v}_{\theta k}\sqrt{\frac{m_j}{m_k}}\right.$$
$$\left.+\frac{1}{2}q\nu_{ionj}^*f_p\hat{v}_{\theta j}\right]+\tilde{n}_j^s\left[-\frac{1}{2}qf_p\hat{v}_{\theta j}^2+\frac{1}{4}q-\frac{1}{2}q\nu_{atj}^*\nu_{ionj}^*\right]$$
$$=-\sum_{k\neq j}\tilde{n}_k^c\left[\frac{1}{2}\varepsilon f_p\nu_{jk}^*\hat{v}_{\theta j}\right]-\frac{1}{4}q\hat{\Phi}_j[\tilde{\Phi}^s]$$
$$-\frac{q^2}{\varepsilon}f_j f_p\left[\frac{1}{2}\{(1+\tilde{\Phi}^c)\hat{v}_{\theta j}-(\hat{v}_{\phi j}-\widehat{P_j'})\tilde{\Phi}^c\}\right]$$
$$-q\hat{v}_{\phi j}^2\left[\frac{1}{4}\varepsilon\{\tilde{v}_{\phi j}^s\tilde{v}_{\phi j}^c+\tilde{n}_j^c\tilde{v}_{\phi j}^s+\tilde{n}_j^s\tilde{v}_{\phi j}^c\}\right]$$
$$-\frac{1}{2}q\nu_{atj}^*[f_p\hat{v}_{\theta j}\tilde{n}_{oj}^c-\nu_{ionj}^*\tilde{n}_{oj}^s]$$
$$-qf_p\nu_{ionj}^*\left[\frac{1}{2}\hat{v}_{\theta j}\left\{\tilde{n}_{oj}^c\left(1+\frac{\overline{n_e}}{\overline{n_j}}\right)\right.\right.$$
$$\left.\left.+\frac{\overline{n_e}}{\overline{nj}}\tilde{n}_e^c\right\}+\frac{1}{3}\frac{q}{\varepsilon}f_j\frac{\overline{n_e}}{\overline{n_j}}(\tilde{n}_e^s+\tilde{n}_{oj}^s)\right], \tag{A12}$$

where

$$\hat{v}_{\theta j}\equiv\frac{\overline{v}_{\theta j}}{|f_p|v_{thj}},\quad \hat{v}_{\phi j}\equiv\frac{\overline{v}_{\phi j}}{v_{thj}},$$

$$\hat{v}_{rj}\equiv\frac{\overline{v}_{rj}}{\left(\frac{m_j v_{thj}}{e_j B_\theta^0}\right)|f_p|\left(\frac{v_{thj}}{qR}\right)},\quad f_p\equiv\frac{B_\theta}{B_\phi},$$

$$\tilde{n}_j^{c/s}\equiv\frac{n_j^{c/s}}{\varepsilon},\quad \tilde{\Phi}^{c/s}\equiv\frac{\Phi^{c/s}}{\varepsilon},\quad \tilde{n}_{oj}^{c/s}\equiv\frac{n_{oj}^{c/s}}{\varepsilon},$$

$$\nu_{jk}^*\equiv\frac{\nu_{jk}}{(v_{thj}/qR)},\quad \nu_{ionj}^*\equiv\frac{\overline{\nu}_{ionj}r}{v_{thj}},\quad \nu_{atj}^*\equiv\frac{\overline{\nu}_{atj}r}{v_{thj}}, \tag{A13}$$

$$\hat{\Phi}_j\equiv\frac{e_j\overline{\Phi}}{T_j},\quad \widehat{P_j'}\equiv\frac{1}{B_\theta^0\overline{n_j}e_j v_{thj}}\frac{\partial p_j}{\partial r}.$$

In order to solve the poloidal moments of the momentum equation described in the previous paragraph, we have used the neoclassical parallel viscosity tensor obtained by extending the classical rate-of-strain tensor formalism to toroidal geometery,[24] leading to the poloidal component of the divergence of the parallel viscosity tensor,

$$\mathbf{n}_\theta\cdot\boldsymbol{\nabla}\cdot\boldsymbol{\pi}=\eta_{oj}\left(\frac{1}{2}A_{oj}\right)\left\{\frac{1}{r}\frac{\partial}{\partial\theta}\frac{\ln(\eta_{oj}A_{oj})}{\partial\theta}\frac{3\sin\theta}{R}\right\}, \tag{A14}$$

where

$$\frac{1}{2}A_{oj}=\left\{-\frac{1}{3}\frac{1}{r}\frac{\partial v_{\theta j}}{\partial\theta}+v_{\theta j}\left(\frac{1}{R}\frac{1}{r}\frac{\partial R}{\partial\theta}+\frac{1}{3}\frac{1}{B_\theta}\frac{1}{r}\frac{\partial B_\theta}{\partial\theta}\right)\right.$$
$$\left.+\left(\frac{B_\theta}{B_\phi}\right)\frac{R}{r}\frac{\partial(v_{\phi j}/R)}{\partial\theta}\right\}, \tag{A15}$$

and by replacing the classical parallel viscosity coefficient with a neoclassical form[25]

$$\eta_{oj}=\frac{n_j m_j v_{thj}qR\varepsilon^{-3/2}\nu_{jj}^*}{(1+\varepsilon^{-3/2}\nu_{jj}^*)(1+\nu_{jj}^*)}\equiv n_j m_j v_{thj}qRf_j(\nu_{jj}^*) \tag{A16}$$

that takes banana-plateau collisionality effects into account.

4. Radial electric field

Finally, we summarize the development of an expression for the radial electric field,[19] which is needed above, by summing the toroidal component of the momentum balance equation over species and making use of the flux surface averaged radial component of the momentum equation

$$\overline{v}_{\phi j}=f_p^{-1}\overline{v}_{\theta j}-(\overline{P_j'}+\overline{\Phi}'), \tag{A17}$$

where

$$f_p\equiv B_\theta/B_\phi,\quad \overline{P_j'}\equiv\frac{1}{\overline{n_j}e_j\overline{B_\theta}}\frac{\partial\overline{p_j}}{\partial r},\quad \overline{\Phi}'\equiv\frac{1}{\overline{B_\theta}}\frac{\partial\overline{\phi}}{\partial r}=-\frac{\overline{E_r}}{\overline{B_\theta}}, \tag{A18}$$

to obtain

$$\frac{E_r}{B_\theta}=\frac{\sum_j^{ions}\{M_{\phi j}+n_j m_j\nu_{dj}^*(P_j'-f_p^{-1}v_{\theta j})\}}{\sum_j^{ions}n_j m_j\nu_{dj}^*}. \tag{A19}$$

APPENDIX B: PENETRATION OF RECYCLING NEUTRALS

The interface-current-balance method[21] is used to calculate the inward transport of a partial current, J_{sol}^+, of neutral particles incident on the scrape-off layer from the divertor and plasma chamber. Defining the albedo as the ratio of inward to outward partial currents, $\alpha_n\equiv J_n^+/J_n^-$, a recursive relation relates the albedos at successive interfaces n

$=1,2,\ldots,N$ numbered successively from the outer boundary of the SOL ($n=1$) inward to the innermost interface ($n=N$):

$$\alpha_n = \frac{\alpha_{n-1}(T_{n-1}^2 - R_{n-1}^2) + R_{n-1}}{1 - \alpha_{n-1}R_{n-1}}, \quad n = 2,3,\ldots,N. \tag{B1}$$

Once the albedos are calculated by sweeping inward from $n=2$ to $n=N$, the ratio of outward partial currents at successive interfaces can be calculated by sweeping outward from $n=N-1$ to $n=1$ using the recursive relation

$$\frac{J_n^-}{J_{n+1}^-} = R_n T_n^{-1}\alpha_{n+1} + (T_n - R_n^2 T_n^{-1}), \quad n = N-1, N-2, \ldots, 1. \tag{B2}$$

The appropriate boundary conditions are $J^+_1 = J^+_{sol}$ and $\alpha_N = \alpha_{\text{plasma}}$. The quantity α_{plasma} is the albedo of a semi-infinite plasma medium, but the actual value is not important if the location of interface N is sufficiently far (several mean free paths) inside the separatrix that the neutral influx is highly attenuated. The quantities R_n and T_n are the reflection and transmission coefficients for the region of thickness $\Delta_n = x_{n+1} - x_n$ with total (ionization + charge-exchange + elastic scattering) mean-free-path λ_n calculated for the local ion and electron temperatures and densities and assuming the neutrals to have the same local temperature as the plasma ions,

$$R_n = \frac{\frac{1}{2}C\left[\frac{\lambda_n}{\Delta_n}\right]\left[\frac{1}{2} - E_3\left(\frac{\Delta_n}{\lambda_n}\right)\right]\left[1 - E_2\left(\frac{\Delta_n}{\lambda_n}\right)\right]}{1 - C\left\{1 - \left[\frac{\lambda_n}{\Delta_n}\right]\left[\frac{1}{2} - E_3\left(\frac{\Delta_n}{\lambda_n}\right)\right]\right\}},$$
$$T_n = E_2\left(\frac{\Delta_n}{\lambda_n}\right) + R_n, \tag{B3}$$

where "C" is the ratio of the charge-exchange plus elastic scattering cross sections to the total cross section, and $E_m(y)$ is the exponential integral function of mth order and of argument "y." The neutral density in each mesh interval is determined by equating the divergence of the neutral current to the ionization rate.

The transmission of uncollided cold neutrals into the edge plasma is calculated from $J^c_{n+1} = E_2(\Delta_n/\lambda^c_n)J^c_n$, where the mean-free-path λ^c is calculated for the temperature of neutrals entering the scrape-off layer from the plenum region.

APPENDIX C: THERMAL CONDUCTIVITY MODELS

1. Neoclassical

The basic neoclassical expression for ion heat conductivity for a two-species (ion-impurity) plasma is

$$\chi_i = \varepsilon^{1/2}\rho_{i\theta}^2 \nu_{iI}, \tag{C1}$$

where $\varepsilon = r/R$ is the ratio of minor and major radii, $\rho_{i\theta}$ is the ion poloidal gyroradius, and ν_{iI} is the ion-impurity collision frequency. A more complete expression is given by the Chang–Hinton formula[26]

$$\chi_i = \varepsilon^{1/2}\rho_{i\theta}^2 \nu_{ii}[a_1 g_1 + a_2(g_1 - g_2)], \tag{C2}$$

where the a's account for impurity, collisionality, and finite inverse aspect ratio effects and the g's account for the effect of the Shafranov shift.

In the presence of a strong shear in the radial electric field E_r, the particle banana orbits are "squeezed," resulting in a reduction in the ion thermal conductivity by a factor of $S^{-3/2}$, where[27]

$$S = \left| 1 - \rho_{i\theta}\left(\frac{d \ln E_r}{dr}\right)\left(\frac{E_r}{\nu_{thi} B_\theta}\right)\right| \tag{C3}$$

ν_{thi} is the ion thermal speed and B_θ is the poloidal magnetic field.

2. Ion temperature gradient mode

For a sufficiently large temperature gradient ($L_{Ti} < L_{Ti}^{crit} \approx 0.1R$—Ref. 28) the toroidal ITG mode becomes unstable. An estimate of the ion thermal conductivity due to ITG modes is given by[29]

$$\chi_i = \frac{5}{2}\left(\frac{1}{RL_{Ti}}\right)^{1/2}\left(\frac{T_e}{m_i}\right)\left(\frac{m_i}{e_i B}\right)\frac{1}{2}\rho_i, \tag{C4}$$

where $k_\perp \rho_i = 2$ has been used, with ρ_i being the ion gyroradius in the toroidal field.

3. Electron drift waves

The principal electron drift wave instabilities with $k_\perp c_s \leqslant \Omega_i$ arise from trapped particle effects when $\nu_e^* = \nu_e/(\nu_{the}/qR)\varepsilon^{3/2} < 1$. In more collisional plasmas the mode becomes a collisional drift wave destabilized by passing particles. An expression for the electron thermal conductivity that encompasses both the dissipative trapped electron mode (TEM) and the transition to the collisionless mode as $\nu_e^* \to 0$ is given by[28]

$$\chi_e = \frac{5}{2}\frac{\varepsilon^{3/2}}{\nu_e}\frac{c_s^2\rho_s^2}{L_n L_{Te}}\left(\frac{1}{1 + 0.1/\nu_e^*}\right), \tag{C5}$$

where c_s is the sound speed and $\rho_s = c_s/\Omega_i$, with Ω_i being the ion cyclotron frequency.

4. Electron temperature gradient modes

The ETG mode (an electron drift wave with $k_\perp c_s \leqslant \omega_{pe}$) is unstable for $\eta_e = L_n/L_{Te} \geqslant 1$. An expression for the electron thermal conductivity associated with the ETG mode is given by[28]

$$\chi_e = 0.13\left(\frac{c_s}{\omega_{pe}}\right)^2 \frac{\nu_{the} S_m}{qR}\eta_e(1 + \eta_e), \tag{C6}$$

where ω_{pe} is the electron plasma frequency and $S_m = (r/q) \times (dq/dr)$ is the magnetic shear.

The turbulent transport models discussed above are analytical simplifications. We use them because we have compared them with experiment[14] for several DIII-D discharges, including the one discussed in this paper. However, neither these nor any other transport models have yet been shown to be valid in the edge pedestal.

[1]M. Kotschenreuther, W. Dorland, Q. P. Liu *et al.*, *Proceedings of 16th Conference Plasma Physics Control Fusion Research, Montreal, 1996* (IAEA, Vienna, 1997), Vol. 2, p. 371.
[2]J. E. Kinsey, R. E. Waltz, and D. P. Schissel, *Proceedings of 24th EPS, Berchtesgarten* (EPS, Petit-Lancy, 1997), Vol. III, p. 1081.
[3]A. E. Hubbard, Plasma Phys. Controlled Fusion **42**, A283 (2000).
[4]R. J. Groebner and T. H. Osborne, Phys. Plasmas **5**, 1800 (1998).
[5]T. H. Osborne, J. R. Ferron, R. J. Groebner *et al.*, Plasma Phys. Controlled Fusion **42**, A175 (2000).
[6]W. Suttrop, O. Gruber, B. Kurzan *et al.*, Plasma Phys. Controlled Fusion **42**, A97 (2000).
[7]T. Onjun, G. Bateman, A. H. Kritz *et al.*, Phys. Plasmas **9**, 5018 (2002).
[8]R. L. Miller, Y. R. Lin-Liu, T. H. Osborne, and T. S. Taylor, Plasma Phys. Controlled Fusion **40**, 753 (1998).
[9]H. R. Wilson and R. L. Miller, Phys. Plasmas **6**, 873 (1999).
[10]J. R. Ferron, M. S. Chu, G. L. Jackson *et al.*, Phys. Plasmas **7**, 1976 (2000).
[11]P. B. Snyder, H. R. Wilson, J. R. Ferron *et al.*, Phys. Plasmas **9**, 2037 (2002).
[12]P. B. Snyder, H. R. Wilson, J. R. Ferron *et al.*, Nucl. Fusion **44**, 320 (2004).
[13]W. M. Stacey, Phys. Plasmas **8**, 4073 (2001).
[14]W. M. Stacey, Phys. Plasmas **11**, 1511 (2004).
[15]W. M. Stacey, Phys. Plasmas **11**, 4295 (2004).
[16]R. J. Groebner, M. A. Mahdavi, A. W. Leonard *et al.*, Phys. Plasmas **9**, 2134 (2002).
[17]W. M. Stacey and R. J. Groebner, Phys. Plasmas **10**, 2412 (2003).
[18]R. J. Groebner, M. A. Mahdavi, A. W. Leonard *et al.*, Nucl. Fusion **44**, 204 (2004).
[19]W. M. Stacey, Phys. Plasmas **11**, 3096 (2004).
[20]W. M. Stacey, Phys. Plasmas **9**, 3874 (2002).
[21]W. M. Stacey, Phys. Plasmas **4**, 179 (1997).
[22]W. M. Stacey, Phys. Plasmas **5**, 1015 (1998); **8**, 3673 (2001).
[23]W. M. Stacey and J. Mandrekas, Nucl. Fusion **34**, 1385 (1994).
[24]W. M. Stacey and D. J. Sigmar, Phys. Fluids **28**, 2800 (1985).
[25]W. M. Stacey, A. W. Bailey, D. J. Sigmar, and K. C. Shiang, Nucl. Fusion **25**, 463 (1985).
[26]C. S. Chang and F. L. Hinton, Phys. Fluids **29**, 3314 (1986).
[27]K. C. Shaing and R. D. Hazeltine, Phys. Fluids B **4**, 2547 (1992).
[28]J. Wesson, *Tokamaks*, 2nd ed. (Clarendon, Oxford, 1997), Sect. 4.18.
[29]F. Romanelli, W. M. Tang, and R. B. White, Nucl. Fusion **26**, 1515 (1986).